ADVANCED FUNCTIONAL MATERIALS
www.afm-journal.de

Photophysics of Organic–Inorganic Hybrid Lead Iodide Perovskite Single Crystals

Hong-Hua Fang, Raissa Raissa, Mustapha Abdu-Aguye, Sampson Adjokatse, Graeme R. Blake, Jacky Even,* and Maria Antonietta Loi**

Hybrid organometal halide perovskites have been demonstrated to have outstanding performance as semiconductors for solar energy conversion. Further improvement of the efficiency and stability of these devices requires a deeper understanding of their intrinsic photophysical properties. Here, the structural and optical properties of high-quality single crystals of $CH_3NH_3PbI_3$ from room temperature to 5 K are investigated. X-ray diffraction reveals an extremely sharp transition at 163 K from a twinned tetragonal I4/mcm phase to a low-temperature phase characterized by complex twinning and possible frozen disorder. Above the transition temperature, the photoluminescence is in agreement with a band-edge transition, explaining the outstanding performances of the solar cells. Whereas below the transition temperature, three different excitonic features arise, one of which is attributed to a free-exciton and the other two to bound excitons (BEs). The BEs are characterized by a decay dynamics of about 5 µs and by a saturation phenomenon at high power excitation. The long lifetime and the saturation effect make us attribute these low temperature features to bound triplet excitons. This results in a description of the room temperature recombination as being due to spontaneous band-to-band radiative transitions, whereas a diffusion-limited behavior is expected for the low-temperature range.

1. Introduction

Solution-processable organic–inorganic hybrid perovskites were reported in the 80s to display a direct bandgap, large absorption coefficient, and strong photoluminescence (PL) as well as high charge-carrier mobility.[1] More recently, $CH_3NH_3PbX_3$ (where X is usually iodine) made its debut as a light-harvesting material for solar cells in 2009,[2] then from 2012 imposed itself by enabling superb power conversion efficiencies both in mesoscopic and in planar heterojunction solar cells.[3–6] Large international efforts to improve the film quality and the device architecture led in a few months to breakthrough performance in thin-film solar cells, with solar-to-electricity conversion efficiencies of over 19%.[7]

Despite the rapid increase in efficiency associated specifically with improved deposition techniques and device architecture, and the importance of a better understanding of the photophysics of the material for further device improvements, only a limited number of works have attempted to gain a thorough understanding of the photophysics of these materials. Most of these few investigations have focused on the nature of the photoexcitations and on the value of the exciton-binding energy. Absorption experiments at low temperature have indicated a binding energy of about 50 meV,[8] which is in agreement with previous reports at $T = 4.2$ K, ranging from 37 to 45 meV.[9,10] The closeness of these values to the room temperature kT made the authors speculate that bound excitons (BEs) and free carriers coexist upon photoexcitation. A recent theoretical study by Even et al.,[11] indicated that these values may be affected by an imprecise determination of the dielectric constant, and depicted a landscape where free carriers are photoexcited at room temperature whereas the Wannier–Mott excitons are dominant at low temperature.[9–11] This is in agreement with recent experimental reports showing room-temperature band-to-band transition and diffusion lengths of up to a micron.[12–15]

Although the nature of the photoexcitations in $CH_3NH_3PbI_3$ appears to have been partially clarified, many questions related to the photoexcitation landscape and transport properties of the pristine perovskite material have been scantily investigated and are poorly understood. An important bottleneck in the investigation of these hybrid perovskites is the variability of their properties not only from lab to lab but also depending on processing conditions. D'Innocenzo et al.[8] have reported inconsistencies of the optical signature of hybrid perovskites that depend on both the crystallinity and support on which the material is deposited.

In this work, we aim to shed light on the excitation landscape and dynamics of the photoexcitations of the model hybrid perovskite $CH_3NH_3PbI_3$ by investigating single-crystal samples. The study of the photoexcitation landscape and of the recombination mechanisms is fundamental to understand

Dr. H.-H. Fang, R. Raissa, M. Abdu-Aguye, S. Adjokatse, Dr. G. R. Blake, Prof. M. A. Loi
Zernike Institute for Advanced Materials
University of Groningen
Nijenborgh 4, Groningen 9747, AG, The Netherlands
E-mail: G.R.Blake@rug.nl; M.A.Loi@rug.nl
Prof. J. Even
Université Européenne de Bretagne
INSA, FOTON
UMR 6082, 35708 Rennes, France
E-mail: Jacky.Even@insa-rennes.fr

DOI: 10.1002/adfm.201404421

and control the loss mechanisms in hybrid perovskite solar cells. Single-crystal measurements are especially important because large variations in the physical properties are related to the microstructure and to small differences in stoichiometry. The single crystals that we synthesized were evidenced to be of high quality by X-ray diffraction. X-ray diffraction also demonstrated an extremely sharp transition at 163 K from a twinned tetragonal I4/mcm phase to a low-temperature phase characterized by complex twinning and possible frozen disorder. Temperature-dependent steady state and time-resolved PL measurements allow the depiction of a complex photoexcitation landscape. Although above the transition temperature, the PL is in agreement with a band-edge transition with a similar temperature dependent shift to the absorption spectra, below the phase transition three different emission peaks arise, one of which we attribute to a free exciton transition and the other two to BEs. The BEs are characterized by a decay dynamics of about 5 µs and by a saturation phenomenon at high pump intensity. The experimental results are discussed in terms of free and bound Wannier excitons at low temperature, whereas a bimolecular band-to-band spontaneous recombination model is in good agreement with the room temperature data. Therefore, the importance of the temperature-dependent induced screening (dielectric constant variation) of the excitons that was theoretically predicted is confirmed.

2. Results and Discussion

2.1. $CH_3NH_3PbI_3$ Single Crystals

Single crystals of $CH_3NH_3PbI_3$ (see inset of **Figure 1**d) were grown as described in Section 4. A few small crystals were selected for optical and X-ray investigations. The space group of $CH_3NH_3PbI_3$ between ≈160 K and ≈340 K was previously reported to be either non-polar I4/mcm or polar I4cm.[16,17] Figure 1a,c present the *h*0*l* and *hk*0 reciprocal lattice planes reconstructed from raw single-crystal X-ray diffraction data collected at 200 K. The sharp spots show the high quality of the crystals. A powder diffraction pattern was collected at room temperature from several crushed crystals and is shown in Figure 1d. The pattern was satisfactorily fitted using the reported I4/mcm structure, and no impurity phases were detected. In the reciprocal lattice images (Figure 1a,c), the reflection condition $h + k + l = 2n$ is obeyed, corresponding to a body-centered lattice. In the *h*0*l* plane (Figure 1a), as previously observed by Baikie et al.,[17] there appear to be reflections that violate the condition for a *c*-glide plane, which is *h*0*l*, $h,l = 2n$. However, this condition holds if pseudo-merohedral twinning is present, forming three domains by successive 120° rotations around the tetragonal $[20\bar{1}]$ axis (the reciprocal $[10\bar{1}]1$ axis, Figure S1c, Supporting Information). Every second reflection along the directions

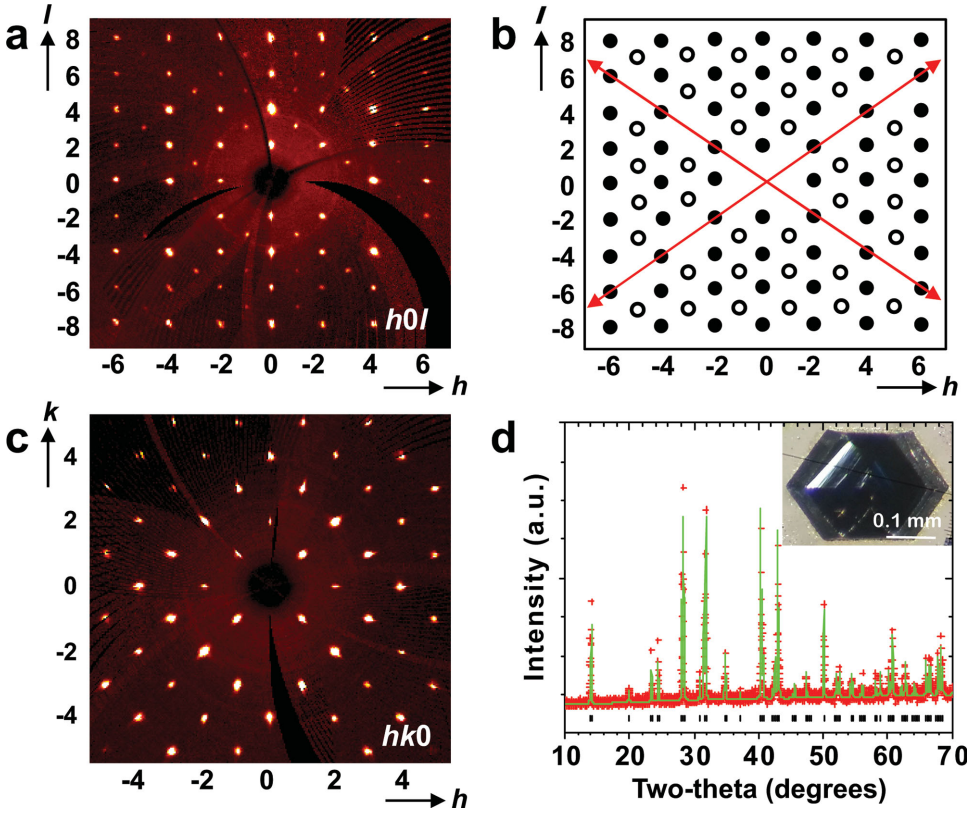

Figure 1. X-ray diffraction patterns of $CH_3NH_3PbI_3$. a) *h*0*l* reciprocal lattice plane reconstructed from raw single crystal diffraction data at 200 K. b) Schematic *h*0*l* reciprocal lattice plane showing reflections formed by superposition of all three twin domains (filled circles) and superposition of two domains (open circles). Red arrows indicate directions in which the reflection condition *h*0*l*, $h,l = 2n$ for a *c*-glide plane is observed. c) *hk*0 reciprocal lattice plane reconstructed from raw single crystal diffraction data at 200 K. d) Measured (red data points) and fitted (green line) powder diffraction patterns obtained from crushed single crystals at room temperature. The black tick marks show the allowed positions of peaks in I4/mcm symmetry. Inset: photograph of a $CH_3NH_3PbI_3$ single crystal.

of the red arrows in Figure 1b is missing; these positions in reciprocal space correspond to *h*0*l* or 0*kl* reflections for which *h* and *l* or *k* and *l* are odd in all three domains. When twinning was introduced, the quality of fit improved significantly. The fit in I4/mcm (RF^2 = 0.0486) was much better than for I4cm (RF^2 = 0.0599). The orientations of the methylammonium (MA) molecules are eight-fold disordered (see Figure S1, Supporting Information), slightly different in geometry to that reported by Kawamura et al.[18] However, the isotropic thermal factors of both atoms are high and the atomic coordinates have relatively large uncertainty, which suggests that the MA molecules retain essentially spherical orientational disorder in the tetragonal phase. Details of the refinement and structure at 200 K are given in the Supporting Information, Table S1 and S2 (Supporting Information).

A sharp phase transition was observed between 163 K and 164 K both on heating and cooling, evidenced by the appearance of new reflections that violate the body-centering condition, as well as by significant changes in intensity and/or splitting of existing peaks. This is apparent in the typical raw detector frame shown in the Figure S2 (Supporting Information). No evidence for an intermediate phase (as postulated by Baikie et al.[17] on the grounds of symmetry) was found. The peak splitting implies that further twin domains are formed below the transition in addition to the three described above; for example, the $00\overline{8}$ reflection in Figure S2 (Supporting Information) splits into a doublet. There is no consensus in the literature on the low-temperature structure of $CH_3NH_3PbI_3$ and as in previous studies,[16] we were unable to find a satisfactory solution. We observed that many peaks develop diffuse features below the transition, which is in agreement with Stoumpos et al.[16] and might correspond to frozen disorder, involving for example the MA rotations.

2.2. Temperature- and Power-Dependent Photoluminescence

In **Figure 2**a, we show a contour map of the temperature dependence of the PL spectra of a $CH_3NH_3PbI_3$ single crystal (inset to Figure 1d) obtained under pulsed laser excitation with a power density of 0.42 μJ cm^{-2}. Figure 2b shows snapshots from this plot taken at different temperatures. The PL spectrum at room temperature is centered at 770 nm and shifts continuously towards the red (805 nm) until about 160 K, in good agreement with the temperature shift of the absorption edge of $CH_3NH_3PbI_3$ thin films.[9,10] The red-shift is accompanied by a reduction of the FWHM.

As discussed in detail in the previous section, a crystallographic phase transition occurs at 163 K–164 K, and a sudden inversion of the trend of the PL is observed below the critical temperature. Between 160 K and 125 K, a blue-shift of the signal occurs, which does not correspond to the red-shift of the absorption spectrum maximum.[8,10] Moreover, at around 100 K, a new band in the PL spectrum appears as a shoulder at about 805 nm, and becomes dominant in the 30–80 K temperature range. When the temperature is further reduced to the 5–30 K range, a simpler PL spectrum characterized by a single peak re-emerges. An increase of two orders of magnitude in the PL intensity is observed between room temperature and 5 K as reported in Figure 2c. Assuming a quantum yield (QY) of 100% at 5 K and a limited temperature-induced variation of the absorption at the excitation wavelength, this results in an estimation of 1% QY at room temperature.

Whereas the red-shift of the PL between 295 K and 160 K is in agreement with the reported temperature dependence of the bandgap of $CH_3NH_3PbI_3$, the complex behavior below 160 K needs careful consideration. Since the phase transition is measured to be extremely sharp, we can rule out the simultaneous presence of two different crystalline phases. A very plausible scenario is the coexistence of at least two excitonic recombinations, whereas only one excitonic transition was predicted previously from absorption spectra.[8–11] It is noteworthy that the low-energy PL maximum (805 nm) in the 30–80 K temperature range is located energetically rather far away from the absorption maximum (740–760 nm).[8]

To further elucidate the nature of the PL below 100 K, we investigated the power dependence of the features described

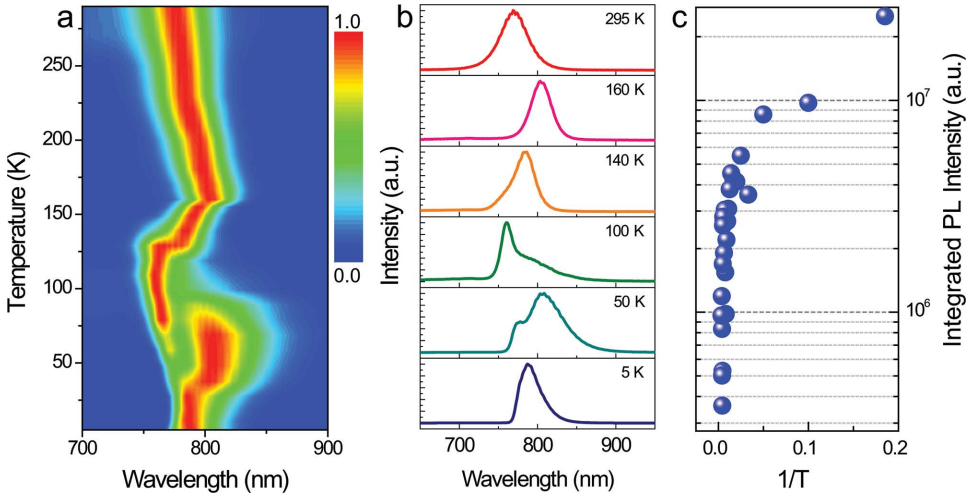

Figure 2. Temperature dependent PL of $CH_3NH_3PbI_3$ single crystal. a) Contour plot of PL spectra of $CH_3NH_3PbI_3$ single crystal at different temperatures under weak excitation density (0.42 μJ/cm^2). b) PL spectra at different temperatures as in (a,c) Integrated PL intensity as a function of temperature.

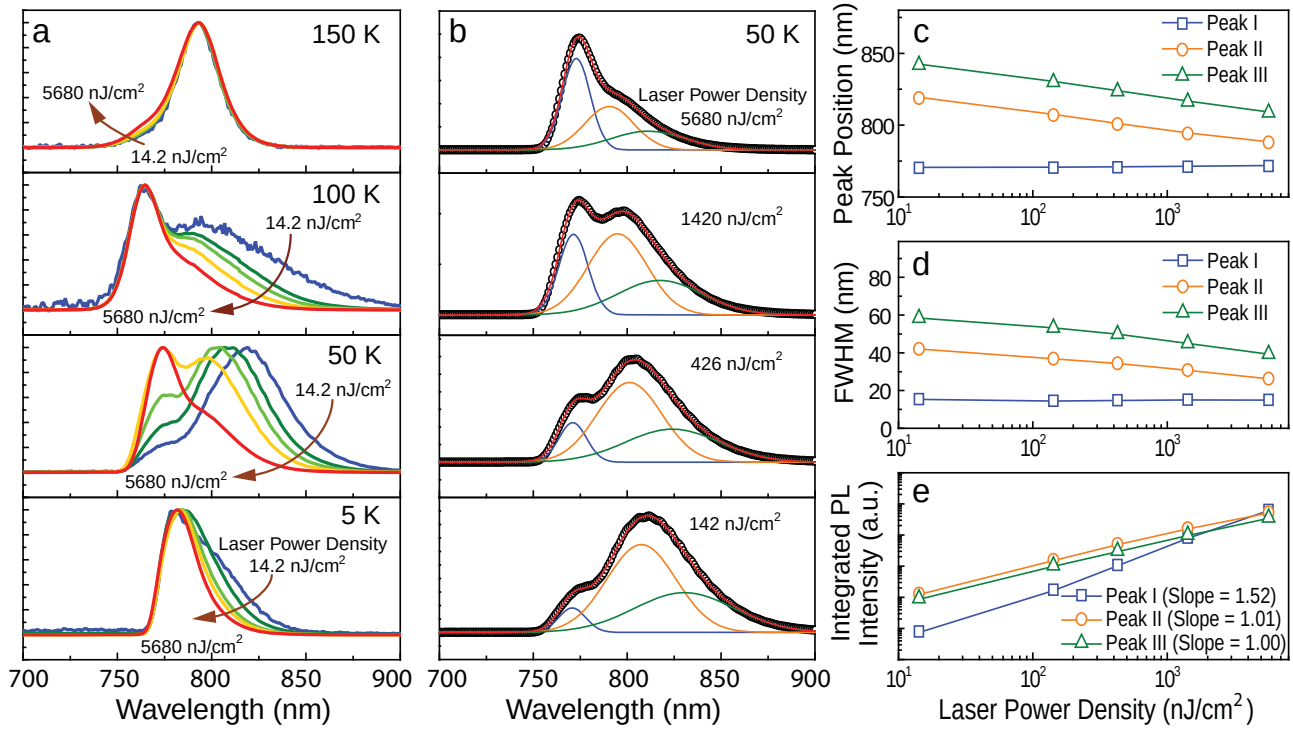

Figure 3. Power dependence of the $CH_3NH_3PbI_3$ single crystal PL at different temperatures. a) PL spectra of the $CH_3NH_3PbI_3$ single crystal at 150 K, 100 K, 50 K, and 5 K are shown in different panels. For each temperature, the laser power density was varied from 14.2 to 5680 nJ cm^{-2}. b) The PL spectra at 50 K measured at different power densities (symbols) are fitted with three Gaussian peaks: peak I (blue), II (orange), and III (green). The overall fits are indicated by the red lines. The following parameters are plotted as a function of power density for each PL peak: c) peak position; d) FWHM; e) Integrated intensity. Data are represented by symbols, whereas lines are guides to the eye in c and d and linear fits in (e).

above. **Figure 3**a shows PL spectra recorded at 150, 100, 50, and 5 K by varying the laser power density from about 14 nJ cm^{-2} to more than 5 mJ cm^{-2}. Already at 150 K, a shoulder at about 760 nm (next to the main PL feature at 793 nm) becomes more prominent as the power density is increased. At 100 K, the relative intensity of the broad low-energy shoulder (805 nm) with respect to the main peak at 765 nm decreases with increasing pump density. At 50 K and low power (14 nJ cm^{-2}), the most prominent peak is at 818 nm, but on increasing the excitation power density the shoulder at 773 nm increases in intensity and becomes the dominant peak when excited with about 5 mJ cm^{-2}. The situation at 5 K is similar, but here the two features are very close (780 nm and 798 nm) and the transfer of intensity is manifested by a decrease in the low-energy tail of the emission at high-power density.

Figure 3b shows the fitting of the power- dependent PL spectra recorded at 50 K. The spectra are well fitted by three Gaussian peaks (Figure 3b), for which the peak positions (Figure 3c), the FWHM (Figure 3d) and the integrated intensities (Figure 3e) for each pump power density are extracted. Figure 3c shows that the high-energy peak (peak I) maintains the same energy with increasing power density whereas the two lower energy peaks (peaks II and III) are blue-shifted.

The increase in intensity of all three emission peaks with laser power (Figure 3e) and the blue-shift (Figure 3c) of the lower energy features can be explained by different mechanisms. First, one can invoke the interplay of an excitonic population (peaks II and III) and a bandedge population (peak I); when the excitonic states become saturated, emission from the band edge will come into play. However, the low-energy peaks have FWHMs (Figure 3d) more than three times larger than that of peak I, which is inconsistent with the assignment of peaks II and III to free excitonic (FE) signatures. On the other hand, peak I exhibits a red-shift on cooling till 150 K (Figure 2), in good agreement with the temperature-dependent shift of the absorption peak maximum.[8–11]

Alternatively, the blue-shift of peaks II and III (Figure 3c) might be due to the filling of trap states and subsequent population of a FE level (peak I). To further analyze the plausibility of this hypothesis, the integrated intensity of each peak was extracted as a function of pump power density, as shown in Figure 3e. Importantly, the slope of the power dependence of the three peaks ranges from 1.5 for peak I to 1.0 for peak III. These slopes are typical for FE transitions or BE transitions (exciton-neutral-donor (D^0X) or exciton-neutral-acceptor (A^0X)) when the excitation is performed with photons of energy above the bandgap,[19] as in our case. In contrast, both free carrier to bound level transitions (hole-neutral-donor (hD^0) or electron-neutral-donor eA^0) and donor-acceptor transitions (D^0A^0) will yield a slope much smaller than 1 with a tendency towards 0.5.[19] It is important to note that FE and BE optical transitions are observed at low temperatures in single crystals of PbI_2.[20] In order to properly investigate our hypothesis of FE and BE transitions in $CH_3NH_3PbI_3$ below T_c, time-resolved PL measurements are essential.

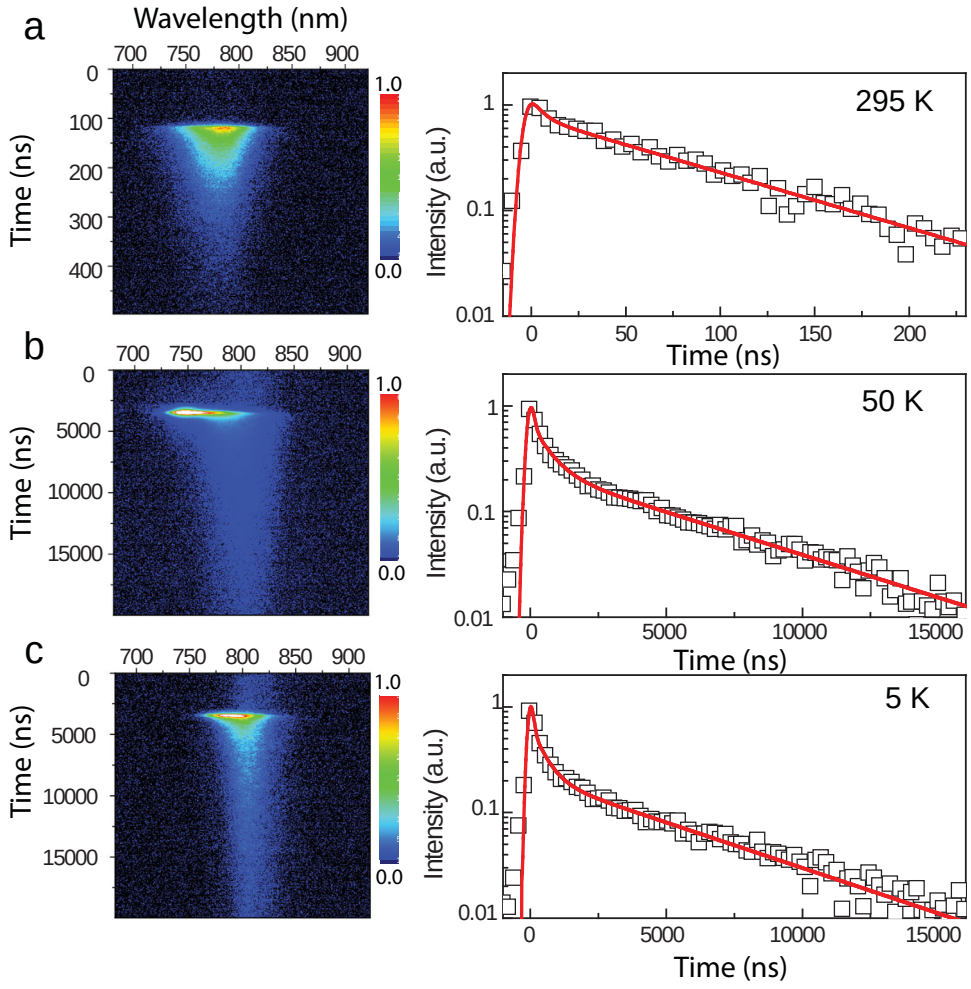

Figure 4. Time-resolved PL emission at different temperatures. a) Streak camera data showing the time-resolved PL emission at 295 K. b) Measurement at 50 K. c) Measurement at 5 K. At all three temperatures, the data were taken in single-sweep mode and the laser excitation density was 1.4 μJ cm^{-2}. For each temperature, the normalized PL decays integrated over all wavelengths are shown next to the original data, and fitting curves are indicated by red lines on top of the experimental data. In (a) the decay at 295 K is fitted with a biexponential function with $t1 = 5.7$ ns (47%), $t2 = 83$ ns (53%). In (b) the decay at 50 K is fitted with $t1 = 375$ ns (80%) and $t2 = 5367$ ns (20%). In (c) the decay at 5 K is fitted with $t1 = 263$ ns (85%) and $t2 = 5043$ ns (15%).

2.3. Time-Resolved Spectroscopy, Excitation Dynamics

We proceed to unravel the dynamics of the complex emission processes at different temperatures using femtosecond-pulsed photoexcitation. **Figure 4** shows streak camera images from room temperature to 5 K, excited with 400 nm excitation pulses at a power density of 1.4 μJ cm^{-2}. At room temperature, the emission spectrum shape is invariant with time. The decay is slightly bi-exponential with a fast component of about 6 ns and a slower one of about 83 ns. The decay becomes slower at lower pump intensity (see Figure S3, Supporting Information) with a lifetime of 124 ns at 0.7 μJ cm^{-2}. This intensity dependence is in agreement with recently reported data on thin films, which were interpreted as indicating bimolecular recombination of free carriers as well as electron and hole trapping.[15,21]

The transient PL spectra are dramatically different below the phase transition temperature. When looking at the streak camera data collected at 50 K, a new ultrafast decay below 800 nm is evident. This is consistent with the appearance in the steady-state spectra of the FE peak named I. The total emission decay is of the order of a few hundreds of ns (limited by the time resolution) and will be analyzed in detail below with higher resolution (**Figure 5**). Beside this component, a new and extremely long-lived emission (peaks II and III) with a lifetime of several microseconds (5.3 μs) is observed. The streak camera data collected at 5 K (Figure 4c) also show a fast component slightly blue-shifted (peak I, as reported in Figure 3) and a very long-lived component decaying in the 5 μs range. Please note that the time resolution of the measurements reported in Figure 4a–c is different because of the different temporal maximum scales (time resolution in single sweep mode is about 1% of the scale).

Figure 5 shows the streak camera data collected at 50 K over a 2 ns time range with a resolution of about 12 ps, which allows us to analyze the fast decay associated with peak I below the transition temperature. The decay of peak I is fitted with an ultrafast component of the order of 200 ps and a slower component of about 2 ns (this latter value is

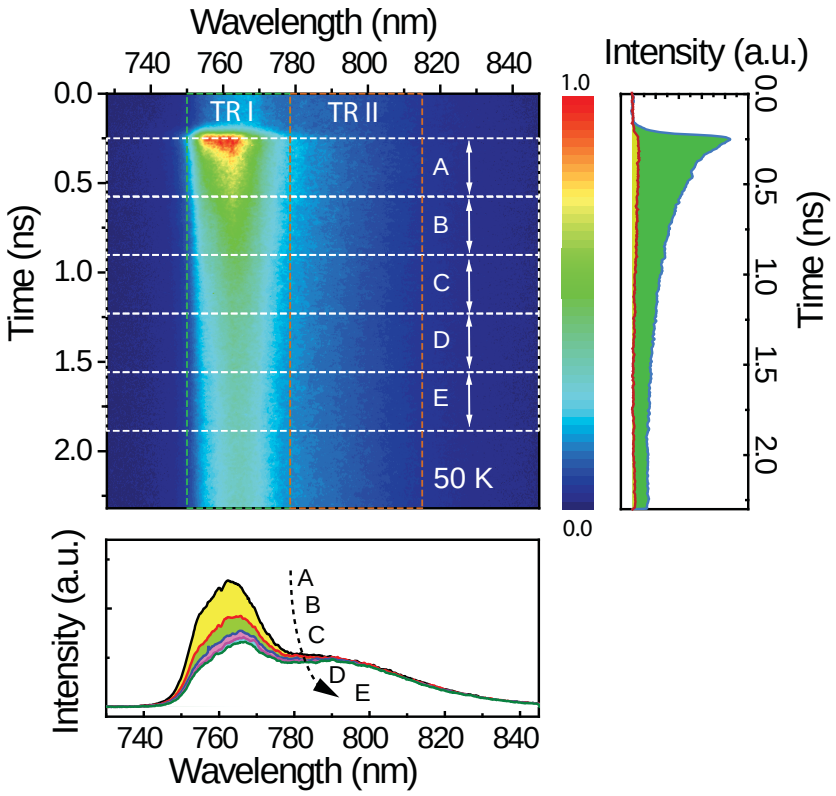

Figure 5. PL dynamics of the fast component at 50 K. The images were taken by streak camera with synchroscan mode exciting the sample with a power density of 1.4 μJ cm^{-2}. The lifetime for TR I can be fitted by biexponential decay with $t_1 = 250$ ps (64%) and $t_2 = 1983$ ps (36%).

underestimated due to the time range of the measurement, which was chosen to detect the fast component; the long-decay component was determined from Figure 4). This initial ultrafast decay, which does not occur for the low-energy features (peaks II and III), can be ascribed to a fast transfer of the excitation population from peak I towards peaks II and III. However, it was not possible to measure the corresponding rise time of peaks II and III in the spectral region indicated as TR II in Figure 5.

As shown by the power-dependent PL data, the low-energy peaks (II and III) may be attributed to BE transitions rather than FE transitions (peak I).[22] The observed long lifetimes are not compatible with a singlet state origin of the emission, neither in inorganic nor in organic semiconductors.

The explanation for the splitting in energy of peak I from peaks II–III involves a singlet to triplet splitting (≈80 meV). However, this value is much larger than the theoretical splitting value (2 meV)[23] for 3D hybrid perovskites, which is close to the experimental splitting in PbI_2.[24] Therefore, the most plausible explanation is that a FE transition is observed at the position of peak I, whereas the triplet state is highly shifted because of its bound state (BE) nature (peaks II and III). In the purely inorganic PbI_2 crystal, the FE-BE splitting measured at low temperature is (≈5 meV)[20] smaller than in $CH_3NH_3PbI_3$, and is related to singlet excitons. However, a similar splitting of the excitonic lines and evidence of triplet excitons was also observed at low temperature in layered hybrid perovskites.[25–27] This large splitting of the excitonic features has been interpreted as competition between FE and BE. We may explain the occurrence of emissive BE triplet states as due to localization caused by site-distribution of the organic cations at low temperature.

It is also interesting to note that when the excitation power is increased at low temperature, although the shorter decay time observed for peak I becomes longer, the BE triplet emission (peaks II and III) becomes faster (from 5.6 to 4.5 ms, see Figure S4b, Supporting Information). The slight increase in lifetime observed for the FE peak (Figure S4a, Supporting Information) with the increase of pump intensity can be determined by the filling of traps acting as non-radiative channels. The nature of these traps and of the neutral sites on which the centers of mass of BE are localized is difficult to identify. Recently, it has been proposed that in thin-films traps are specially localized at the grain boundaries,[28] but in our case we can speculate that the surface of our crystal is the main location of the traps.

Since the spontaneous emission rate of excitonic features is generally proportional to the population, shortening of the decay times at high-power intensity in the case of the BE feature (Figure S4b, Supporting Information) might be related to the influence of specific many-body effects, such as triplet–triplet annihilation.

2.4. Theoretical Description of the Recombination Dynamics

Our previous study has shown the importance of the spin-orbit coupling effect in the conduction band (CB), leading to optical recombination between a nondegenerate spin-orbit split-off CB and a nondegenerate valence band (VB).[29] This situation is simpler than in III–V semiconductor materials where great care should be taken to account for VB degeneracy as well as the balance between VB spin-orbit coupling energy and the electronic bandgap. Here, we compute the spontaneous bimolecular optical recombination rate at room temperature using a band-to-band mechanism:[30,31]

$$R_{sp}(\hbar\omega) = \frac{2C_0}{V} G(\hbar\omega) \sum_{k_{CB}} \sum_{K_{VB}} \left|\vec{e}.\vec{p}_{cv}\right|^2 \delta(E_{CB} - E_{VB} - \hbar\omega)$$
$$\delta(\vec{k}_{CB} - \vec{k}_{VB} - \vec{k}_{opt}) f_{CB}(1 - f_{VB})$$

where $G(\hbar\omega)$ represents the optical density of states, f_{CB} and f_{VB} are the electronic band populations, C_0 is a constant, and $\left|\vec{e}.\vec{p}_{cv}\right|^2$ is the oscillator strength of the transition related to CB

and VB Bloch functions. After averaging over light polarization, the oscillator strength yields $\frac{m_0 E_p}{6}$ where the standard Kane energy of conventional III–V E_p appears as a key parameter. A Kane energy equal to 6.3 eV was calculated for $CH_3NH_3PbI_3$ in our previous density functional theory (DFT) study.[11] This value is a little smaller than the one (23–25 eV) reported for GaAs but of the same order as that (5.5 eV) computed for layered hybrid perovskites.[32] The total spontaneous emission rate is obtained by considering parabolic electronic dispersions in the CB and VB and integrating $R_{sp}(\hbar\omega)$:[30,31]

$$R_{sp} = \int R_{sp}(\hbar\omega)\mathrm{d}(\hbar\omega) = Bnp$$

Here the bimolecular recombination rate **B** is given by $B = \frac{1}{(m_{CB}+m_{VB})^{3/2}} C(E_g, T, E_p)$, which depends on the CB and VB effective masses and on a function **C**, dependent on temperature, the Kane energy, and electronic bandgap. Assuming effective masses equal to 0.15 and 0.12 in the CB and VB, respectively, the formula yields a bimolecular recombination rate equal to 1.1×10^{-10} s^{-1} cm^3 at room temperature, in good agreement with the experimental values of 1.7×10^{-10} s^{-1} cm^3 and 1.3×10^{-10} $s^{-1}cm^3$ in previous studies,[15,21] but smaller than other experimental values (9.4×10^{-10} s^{-1} cm^3, 13×10^{-10} s^{-1} cm^3, and 2.3×10^{-9} s^{-1} cm^3) reported, respectively, in previous studies.[33–35] As quoted by Ishihara et al.,[25] the experimental determination of the B value strongly depends on the minimization of carrier trapping, and thus the crystalline quality of the sample.

We note that a fundamental understanding of the room temperature recombination process is crucial, since large mobilities and reduced recombinations are important for the development of efficient photovoltaic devices. Room temperature experimental results have been discussed up to now within the framework of the diffusion-limited bimolecular recombination model, widely used for the analysis of organic solar cells. However, available experimental results for hybrid perovskites, including the present work, are several orders of magnitude lower than expected from the Langevin theory.[21,34,36] This paradox is solved when one rather considers spontaneous radiative emission as the limiting process for bimolecular recombination. Good transport properties as well as efficient light emission are indeed simultaneously observed in the case of III–V semiconductors like GaAs, InAs, or InP. The good agreement obtained with the experimental values is consistent with a picture where electronic excitations involve Bloch electronic states.[11,29,32] The bimolecular recombination rate of hybrid perovskites is then related to the values of the effective masses, both in the CB and VB, and to the large value of the Kane energy, although this parameter is a little smaller than in conventional III–V semiconductors. Since low-temperature optical measurements exhibit clear FE and BE signatures, we may expect that the diffusion-limited approach is still relevant for this temperature range.

The FE spontaneous emission time τ_r relevant for the low-temperature phase dynamics can be estimated from the recombination rate computed at the band edge:[31]

$$R_{sp} = \frac{1}{\tau_r} = \frac{e^2 n_r E_p E_{gap}}{6\pi\varepsilon_0 m_0 c^3 \hbar^2}$$

This approximate formula yields a spontaneous emission time equal to 2.7 ns for $CH_3NH_3PbI_3$ and 0.6 ns for GaAs at the same level of theory. The lifetime of the FE of $CH_3NH_3PbI_3$ appears to be underestimated. However, precise modeling of the FE spontaneous emission time would require a complete determination of the excitonic enhancement of the optical absorption as well as the broadening mechanism.

3. Conclusion

The temperature-dependent structural and optical properties of high-quality single crystals of $CH_3NH_3PbI_3$ have been investigated. X-ray diffraction demonstrated an extremely sharp transition at 163 K from a twinned tetragonal I4/mcm phase to a low-temperature phase characterized by complex twinning and possible frozen disorder. Temperature-dependent steady-state and time-resolved PL allow the depiction of a complex photoexcitation landscape. Whereas above the transition temperature, the PL is in agreement with a band-edge transition with a similar temperature-dependent shift to the absorption spectra, below the phase transition three different emission peaks arise, one of which is attributed to a free-exciton transition and the other two peaks to bound excitons. The bound excitons are characterized by a decay dynamics of about 5 µs and by a saturation phenomenon at high pump intensity. We attribute this extremely long lifetime to the BEs having a triplet-state nature. This not only clarifies the photoexcitation landscape of hybrid perovskites but also has large relevance for the future development of optoelectric devices (e.g., Lasers). The importance of the previously predicted temperature-induced screening is experimentally confirmed. Finally, the photophysics of hybrid perovskite materials is compared in this work to that of conventional III–V semiconductors, giving great hope for what to expect for future solar cell efficiencies.

4. Experimental Section

Materials Preparation: MAI was synthesized by mixing 24 mL methylamine (33% in ethanol) and 10 mL HI (57% in water) in 100 mL ethanol (in an ice bath) with constant stirring for 2 h. After evaporation at 60 °C on a hotplate, the resulting white powder was washed three times with ethyl ether and dried in vacuum at 60 °C overnight. Equimolar mixtures of PbI_2 and MAI in gamma-butyrolactone were left to stir overnight at 60 °C, yielding a homogeneous yellow solution. Single crystals were obtained by drop casting the solution on glass substrates, which were heated at 100 °C for 20 min.

X-Ray Diffraction: Powder X-ray diffraction data were collected using a Bruker D8 Advance diffractometer in Bragg-Brentano geometry and operating with Cu Kα radiation. The data were fitted using the GSAS software.[37] Single-crystal X-ray diffraction was performed using a Bruker D8 Venture diffractometer operating with Mo Kα radiation and equipped with a Triumph monochromator and a Photon100 area detector. The sample was mounted in a nylon loop using cryo-oil and cooled using a nitrogen flow from an Oxford Cryosystems Cryostream Plus. The data were processed using the Bruker Apex II software. The structure was solved and refined using the SHELXTL software.[38]

Optical Spectroscopy: For the PL measurement, the samples were excited at approximately 400 nm by the second harmonic of a mode-locked Ti:Sapphire laser (Mira 900, Coherent) or a 405 nm continuous wave laser diode. The laser power was controlled by a variable neutral density filter. To vary the repetition rate of the exciting pulses, an optical pulse selector was used. For low-temperature steady-state and time-resolved PL measurements, the crystals were sandwiched between quartz substrates and loaded into a continuous flow helium cryostat (Optistat Oxford). The PL decays were recorded by a Hamamatsu streak camera working in single sweep or a synchro-scan mode. The instrument response function was varied between 2 ps (synchroscan mode) and several ns (1% of the temporal window in single sweep mode) depending on the time range of the specific experiment. The PL spectra were corrected for the spectral response of the setup using a calibrated light source.

Fitting and Data Analysis for Optical Measurements: Steady-state spectra are fitted with Gaussian functions (the average goodness-of-fit was determined by the chi squared (χ^2) test). Lifetimes were fitted using exponential functions such as $I = \sum_i A_i \exp(-t/\tau_i)$. When only one lifetime is reported, the best fit could be achieved with a mono-exponential function; otherwise a bi-exponential function was used.

Supporting Information

Supporting Information is available from the Wiley Online Library or from the author.

Acknowledgements

The work in Groningen was partially supported by the European Research Council, ERC Starting Grant (No. 306983) "Hybrid solution processable materials for opto-electronic devices" (ERC-HySPOD) and by the Foundation for Fundamental Research on Matter (FOM), which is part of the Netherlands Organization for Scientific Research (NWO), under the framework of the FOM Focus Group "Next Generation Organic Photovoltaics". The authors would like to thank T. T. M. Palstra, S. Z. Bisri, and R. W. A. Havenith for inspiring discussions. The technical support of A. Kamp, J. Baas, and J. Harkema is gratefully acknowledged. The list of authors in Reference 14 was amended on April 22, 2015.

Received: December 13, 2014
Revised: January 19, 2015
Published online: February 13, 2015

[1] D. B. Mitzi, *Prog. Inorg. Chem.* **2007**, *48*, 1.
[2] A. Kojima, K. Teshima, Y. Shirai, T. Miyasaka, *J. Am. Chem. Soc.* **2009**, *131*, 6050.
[3] M. M. Lee, J. Teuscher, T. Miyasaka, T. N. Murakami, H. J. Snaith, *Science* **2012**, *338*, 643.
[4] H.-S. Kim, C.-R. Lee, J.-H. Im, K.-B. Lee, T. Moehl, A. Marchioro, S.-J. Moon, R. Humphry-Baker, J.-H. Yum, J. E. Moser, *Sci. Rep.* **2012**, *2*, 591.
[5] J. Burschka, N. Pellet, S.-J. Moon, R. Humphry-Baker, P. Gao, M. K. Nazeeruddin, M. Grätzel, *Nature* **2013**, *499*, 316.
[6] M. Liu, M. B. Johnston, H. J. Snaith, *Nature* **2013**, *501*, 395.
[7] H. Zhou, Q. Chen, G. Li, S. Luo, T.-B. Song, H.-S. Duan, Z. Hong, J. You, Y. Liu, Y. Yang, *Science* **2014**, *345*, 542.
[8] V. D'Innocenzo, G. Grancini, M. J. Alcocer, A. R. S. Kandada, S. D. Stranks, M. M. Lee, G. Lanzani, H. J. Snaith, A. Petrozza, *Nat. Commun.* **2014**, *5*, 3586.
[9] M. Hirasawa, T. Ishihara, T. Goto, K. Uchida, N. Miura, *Phys. B* **1994**, *201*, 427.
[10] T. Ishihara, *J. Lumin.* **1994**, *60*, 269.
[11] J. Even, L. Pedesseau, C. Katan, *J. Phys. Chem. C* **2014**, *118*, 11566.
[12] S. D. Stranks, G. E. Eperon, G. Grancini, C. Menelaou, M. J. Alcocer, T. Leijtens, L. M. Herz, A. Petrozza, H. J. Snaith, *Science* **2013**, *342*, 341.
[13] G. Xing, N. Mathews, S. Sun, S. S. Lim, Y. M. Lam, M. Grätzel, S. Mhaisalkar, T. C. Sum, *Science* **2013**, *342*, 344.
[14] M. Saba, M. Cadelano, D. Marongiu, F. Chen, V. Sarritzu, N. Sestu, C. Figus, M. Aresti, R. Piras, A. G. Lehmann, C. Cannas, A. Musinu, F. Quochi, A. Mura, G. Bongiovanni, *Nat. Commun.* **2014**, *5*, 5049.
[15] Y. Yamada, T. Nakamura, M. Endo, A. Wakamiya, Y. Kanemitsu, *J. Am. Chem. Soc.* **2014**, *136*, 11610.
[16] C. C. Stoumpos, C. D. Malliakas, M. G. Kanatzidis, *Inorg. Chem.* **2013**, *52*, 9019.
[17] T. Baikie, Y. Fang, J. M. Kadro, M. Schreyer, F. Wei, S. G. Mhaisalkar, M. Graetzel, T. J. White, *J. Mater. Chem. A* **2013**, *1*, 5628.
[18] Y. Kawamura, H. Mashiyama, K. Hasebe, *J. Phys. Soc. Jpn.* **2002**, *71*, 1694.
[19] T. Schmidt, K. Lischka, W. Zulehner, *Phys. Rev. B* **1992**, *45*, 8989.
[20] F. Levy, A. Mercier, J.-P. Voitchovsky, *Solid State Commun.* **1974**, *15*, 819.
[21] S. D. Stranks, V. M. Burlakov, T. Leijtens, J. M. Ball, A. Goriely, H. J. Snaith, *Phys. Rev. Appl.* **2014**, *2*, 034007.
[22] P. Y. Yu, M. Cardona, *Fundamentals of semiconductors: Physics and Materials Properties[M]*, Springer, Berlin **2005**.
[23] M. Hirasawa, T. Ishihara, T. Goto, *J. Phys. Soc. Jpn.* **1994**, *63*, 3870.
[24] Y. Nagamune, S. Takeyama, N. Miura, *Phys. Rev. B* **1991**, *43*, 12401.
[25] T. Ishihara, J. Takahashi, T. Goto, *Phys. Rev. B* **1990**, *42*, 11099.
[26] N. Kitazawa, M. Aono, Y. Watanabe, *J. Phys. Chem. Solids* **2011**, *72*, 1467.
[27] T. Goto, H. Makino, T. Yao, C. Chia, T. Makino, Y. Segawa, G. A. Mousdis, G. C. Papavassiliou, *Phys. Rev. B* **2006**, *73*, 115206.
[28] Y. Shao, Z. Xiao, C. Bi, Y. Yuan, J. Huang, *Nat. Commun.* **2014**, *5*, 5784.
[29] J. Even, L. Pedesseau, J.-M. Jancu, C. Katan, *J. Phys. Chem. Lett.* **2013**, *4*, 2999.
[30] S. L. Chuang, *Physics of Optoelectronic Devices*, (Ed: J. W. Goodman), Wiley, New York **1995**.
[31] P. K. Basu, *Theory of Optical Processes in Semiconductors: Bulk and Microstructures: Bulk and Microstructures[M]*, Oxford University Press, Oxford **1997**.
[32] J. Even, L. Pedesseau, M.-A. Dupertuis, J.-M. Jancu, C. Katan, *Phys. Rev. B* **2012**, *86*, 205301.
[33] J. S. Manser, P. V. Kamat, *Nat. Photonics* **2014**, *8*, 737.
[34] T. J. Savenije, C. S. Ponseca, L. T. Kunneman, M. A. Abdellah, K. Zheng, Y. Tian, Q. Zhu, S. E. Canton, I. G. Scheblykin, T. Pullerits, *J. Phys. Chem. Lett.* **2014**, *5*, 2189.
[35] A. Beattie, P. Landsberg, *Proc. R. Soc. Lond. A* **1959**, *249*, 16.
[36] C. Wehrenfennig, G. E. Eperon, M. B. Johnston, H. J. Snaith, L. M. Herz, *Adv. Mater.* **2014**, *26*, 1584.
[37] R. Von Dreele, A. Larson, *Los Alamos Natl. Lab. Rep.* **2004**, *86*, 86.
[38] G. M. Sheldrick, *Acta Cryst. A* **2007**, *64*, 112.